

SPICE: Self-Supervised Learning for MRI with Automatic Coil Sensitivity Estimation

Yuyang Hu^{*,1}, Weijie Gan^{*,2}, Chunwei Ying⁴, Tongyao Wang³, Cihat Eldeniz⁴,
Jiaming Liu¹, Yasheng Chen⁵, Hongyu An^{1,3,4,5}, Ulugbek S. Kamilov^{1,2}

¹Department of Electrical & System Engineering, Washington University in St. Louis, St. Louis

²Department of Computer Science & Engineering, Washington University in St. Louis, St. Louis

³Department of Biomedical Engineering, Washington University in St. Louis, St. Louis

⁴Mallinckrodt Institute of Radiology, Washington University in St. Louis, St. Louis

⁵Department of Neurology, Washington University in St. Louis, St. Louis

*These authors have contributed equally to the work

Abstract

Deep model-based architectures (DMBAs) integrating physical measurement models and learned image regularizers are widely used in parallel magnetic resonance imaging (PMRI). Traditional DMBAs for PMRI rely on pre-estimated coil sensitivity maps (CSMs) as a component of the measurement model. However, estimation of accurate CSMs is a challenging problem when measurements are highly undersampled. Additionally, traditional training of DMBAs requires high-quality groundtruth images, limiting their use in applications where groundtruth is difficult to obtain. This paper addresses these issues by presenting SPICE as a new method that integrates self-supervised learning and automatic coil sensitivity estimation. Instead of using pre-estimated CSMs, SPICE simultaneously reconstructs accurate MR images and estimates high-quality CSMs. SPICE also enables learning from undersampled noisy measurements without any groundtruth. We validate SPICE on experimentally collected data, showing that it can achieve state-of-the-art performance in highly accelerated data acquisition settings (up to $10\times$).

1 Introduction

Magnetic resonance imaging (MRI) is a medical imaging technology known to suffer from slow data acquisition. *Parallel MRI (PMRI)* is a widely-used acceleration strategy that relies on the spatial encoding provided by multiple receiver coils to reduce the amount of data to acquire [1–4]. To combine multi-coil data into a single image, PMRI requires the calibration of coil sensitivities. Calibration can be performed either in k-space [1, 2] or in the image space using *coil sensitivity maps (CSMs)* [3, 4]. *Compressed sensing (CS)* is a complementary technique used to further accelerate data collection by using prior knowledge on the unknown image (sparsity, low-rankness) [5, 6].

Deep learning (DL) has recently emerged as a promising paradigm for image reconstruction in CS-PMRI [7–9]. Traditional DL methods train *convolutional neural networks (CNNs)* to map acquired measurements to the desired images [10, 11]. Recent work has shown that *deep model-based architectures (DMBAs)* can perform better than generic CNNs by accounting for the measurement model of the parallel imaging system [12–17]. Most of these methods require pre-calibrated CSMs as an important element in their model. However, CSM pre-estimation strategies rely on sufficient *auto-calibration signal (ACS)* lines, which limits the acceleration rates for data acquisition. To address this limitation, recent work has proposed to jointly estimate high-quality images and CSMs in an end-to-end manner [18–20]. However, these methods still require fully-sampled groundtruth images as training targets, which limits their applicability to settings where groundtruth is difficult to obtain or unavailable. On the other hand, there has also been a broad interest in developing self-supervised DL methods that rely exclusively on the information available in the undersampled measurements [17, 21–26].

Despite the rich literature on DMBAs and self-supervised DL, the existing work in the area has not investigated joint image reconstruction and coil sensitivity estimation directly from noisy and undersampled data. We bridge this

gap by presenting *Self-Supervised Learning for MRI with Automatic Coil Sensitivity Estimation (SPICE)* as a new self-supervised learning framework for parallel MRI that is equipped with an automatic CSM estimator. SPICE is a synergistic combination of a powerful model-based architecture and a flexible self-supervised training scheme. The SPICE architecture consists of two branches: (a) a CNN for estimating CSMs from possibly limited ACS data, while ensuring physically realistic predictions (see Fig 5); (b) a DMBA that uses the estimated CSMs for high-quality image reconstruction. The SPICE training is performed directly in k-space using undersampled and noisy measurements without any fully-sampled groundtruth. For training, SPICE only requires a pair of undersampled and noisy measurements from the same object. We extensively validated SPICE on *in-vivo* MRI data for several acceleration factors. Our results show that SPICE can achieve state-of-the-art performance on PMRI at high acceleration rates (up to $10\times$). Moreover, SPICE can estimate better CSMs than pre-estimation methods especially when the ACS data is limited.

This paper extends the preliminary work presented in the workshop paper [27]. Compared to the method in [27], SPICE uses a different forward model, model-based deep learning architecture, and training loss function. This paper also provides an expanded discussion on related work, additional technical details, as well as completely new numerical results using real *in-vivo* MRI data acquired using 32 coils.

2 Background

2.1 Problem Formulation

Consider the following CS-PMRI measurement model

$$\mathbf{y} = \mathbf{A}\mathbf{x} + \mathbf{e}, \quad (1)$$

where $\mathbf{x} \in \mathbb{C}^n$ is an unknown image, $\mathbf{y} = (\mathbf{y}_1, \dots, \mathbf{y}_{n_c})$ are the multi-coil measurements from $n_c \geq 1$ coils, $\mathbf{e} = (\mathbf{e}_1, \dots, \mathbf{e}_{n_c})$ is the noise vector, and $\mathbf{A} = (\mathbf{A}_1, \dots, \mathbf{A}_{n_c})$ is the measurement operator (or forward operator). The measurement model for each coil can be represented as

$$\mathbf{y}_k = \underbrace{\mathbf{P}\mathbf{F}\mathbf{S}_k}_{\mathbf{A}_k} \mathbf{x} + \mathbf{e}_k, \quad k = 1, 2, \dots, n_c, \quad (2)$$

where $\mathbf{S}_k \in \mathbb{C}^{n \times n}$ is the CSM of the k th coil, $\mathbf{F} \in \mathbb{C}^{n \times n}$ is the Fourier transform operator, $\mathbf{P} \in \mathbb{C}^{n \times n}$ is the k-space sampling operator, and $\mathbf{e} \in \mathbb{C}^n$ is the noise vector. Note that $\mathbf{S} = (\mathbf{S}_1, \dots, \mathbf{S}_{n_c})$ varies for each scan, since it depends on the relative location of the coils with the object being imaged. When \mathbf{S} are known, image reconstruction can be formulated as regularized optimization

$$\hat{\mathbf{x}} = \arg \min_{\mathbf{x}} f(\mathbf{x}) \quad \text{with} \quad f(\mathbf{x}) = g(\mathbf{x}) + h(\mathbf{x}), \quad (3)$$

where g is the data fidelity term that quantifies consistency with the observed data \mathbf{y} and h is a regularizer that infuses prior knowledge on \mathbf{x} . Examples of g and h used in CS-PMRI are the least-squares and *total variation (TV)* functions [28]

$$g(\mathbf{x}) = \frac{1}{2} \|\mathbf{A}\mathbf{x} - \mathbf{y}\|_2^2 \quad \text{and} \quad h(\mathbf{x}) = \tau \|\mathbf{D}\mathbf{x}\|_1, \quad (4)$$

where \mathbf{D} denotes the image gradient and $\tau > 0$ is a regularization parameter.

DL has recently gained popularity in MRI image reconstruction due to its excellent empirical performance [7, 8, 29]. Traditional DL methods are based on training CNNs (such as U-Net [30]) to map the corrupted images [31, 32] or the under-sampled measurements [33, 34] to their desired fully sampled ground-truth versions. There is also growing interest in DMBA that can combine physical measurement models and learned CNN priors. Well known examples of DMBA are *plug-and-play priors (PnP)* [35, 36], *regularized by denoising (RED)* [37], and *deep unfolding (DU)* [38–40]. In particular, DU has gained notoriety due to its ability to achieve the state-of-the-art performance, while providing robustness to changes in data acquisition. DU architectures are typically obtained by unfolding iterations of an image reconstruction algorithm as layers, representing the regularizer within image reconstruction as a CNN, and training the resulting network end-to-end. Different DU architectures can be obtained by using various optimization/reconstruction algorithms. In this paper, we will rely on a DU variant of the RED model as the basis of our image reconstruction method [41].

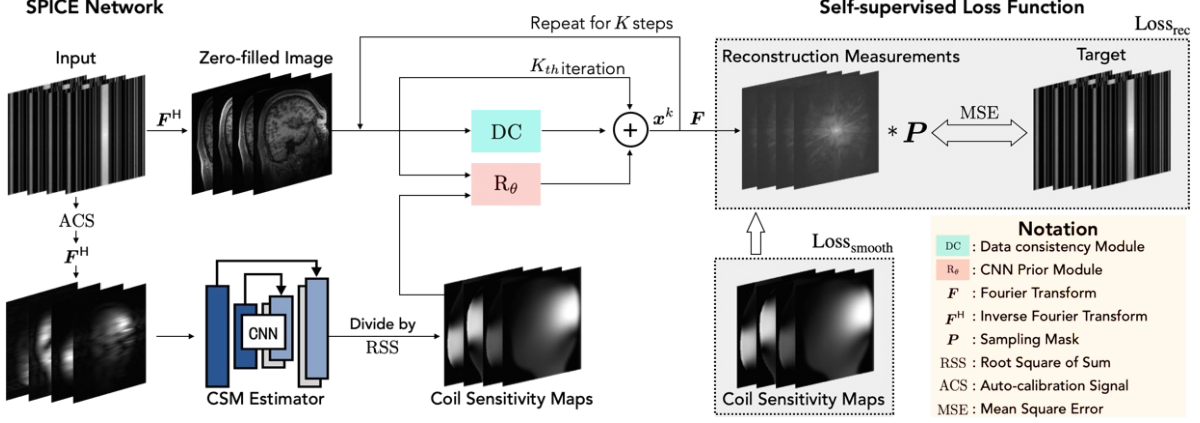


Figure 1: The SPICE method consists of a DMBA-based MRI reconstruction module and a coil sensitivity estimation module that map multicoil undersampled measurements to a single high-quality image and a set of coil sensitivity maps, respectively. The network is trained directly on raw k-space measurements where the input and the target measurement correspond to a pair of undersampled measurements from the same object.

2.2 Reconstruction using Pre-Calibrated CSMs

There are two widely-used image formation approaches in CS-PMRI (see recent review [8]): (a) reconstruction in the k-space domain and (b) reconstruction in the image domain. GRAPPA [2] is a well-known example of (a) that fills in unacquired k-space values by linearly interpolating acquired neighboring k-space samples. Recent work [42] extends GRAPPA by using a CNN to learn a non-linear interpolator in k-space. SENSE [3] and ESPIRiT [4] are two well-known examples of (b) that first pre-calibrate \mathbf{S} and then use it to solve the inverse problem (1). Our work in this paper adopts strategy (b), which will be the focus of the subsequent discussion.

Pre-estimated CSMs can either be obtained by doing a separate calibration scan [43] or estimated directly from the ACS region of the undersampled measurements. The drawback of the former approach is that it extends the total scan time. ESPIRiT [4] is based on the latter approach. There are several issues and challenges with the pre-estimated approaches [43, 44]. One issue is that the inconsistencies between the calibration scan and the accelerated scan can result in imaging artifacts. Another issue is that estimating CSMs from a small number of ACS lines may not be sufficiently accurate. DeepSENSE [45], a recent supervised DL method, uses a CNN to learn a mapping from the ACS data to calibration scans, which are used as CSM groundtruths. DeepSENSE achieves improves over pre-estimated methods, especially with limited ACS data. However, the groundtruth CSMs used in DeepSENSE are hard to acquire in practice.

2.3 Joint Reconstruction and CSM estimation

Traditionally, optimization-based methods for joint image reconstruction and CSM estimation treat \mathbf{S} as another unknown variable in (3) and alternate between updating the image and updating the coil sensitivities [43, 44]. Deep unfolding has recently been adopted to perform joint estimation of image and CSMs without any pre-calibration procedure [18–20, 46]. The concept behind these methods is to model CSM estimated as a trainable DNN module that can be optimized simultaneously with other learnable parameters in the deep network. The inputs to the CSM estimated modules could be the original undersampled measurements [20] or the intermediate results available at different layers of the deep unfolded networks [18, 19]. However, these joint learning methods rely on fully-sampled groundtruth images as training targets, which limits their applicability when groundtruth data is not available. Our work contributes to this area by investigating a self-supervised learning approach for joint image reconstruction and CSM calibration that requires no fully-sampled groundtruth data.

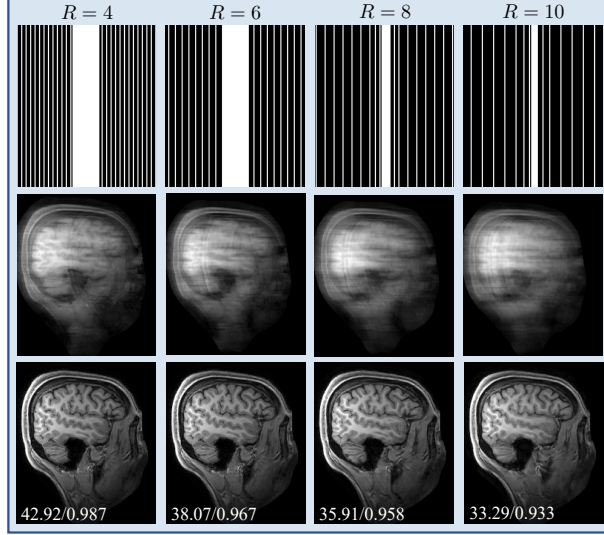


Figure 2: The first row shows the cartesian equispaced sampling masks P used in the experimental validation: $R = 4, 6, 8$ and 10 , with corresponding ACS lines = $24, 24, 8$ and 5 . The second row shows the zero-filled images of the same slice for the four acceleration rates. The third row shows the SPICE reconstructed images of the same slice and include the PSNR/SSIM values with respect to the groundtruth.

2.4 Self-supervised Image Reconstruction

There is a growing interest in DL-based image reconstruction to reduce the dependence of training on high-quality ground-truth data (see recent reviews [47–49]). Some well-known strategies include *Noise2Noise* (N2N) [50], *Noise2Void* (N2V) [51], *deep image prior* (DIP) [52], *Compressive Sensing using Generative Models* (CSGM) [53], and equivariant imaging [54]. This work is most related to N2N, where a DNN R_θ is trained on a set of noisy images $\{\hat{x}_{i,j} = x_i + e_{i,j}\}$ with j indexing different realizations of the same underlying image i . The N2N learning is formulated as follows

$$\hat{\theta} = \arg \min_{\theta} \sum_i \sum_{j \neq j'} \|f_\theta(y_{i,j}) - y_{i,j'}\|_2^2, \quad (5)$$

where f_θ denotes a CNN with θ being trainable parameters. N2N and its extensions have been investigated in several papers on PMRI reconstruction [24–26]. For example, DURED-Net [55] proposes an unsupervised learning method for MRI image reconstruction combining an unsupervised denoising network and a PnP method. A related idea, known as SSDU [17], trains a DU model without groundtruth by dividing a single k-space MRI acquisition into two subsets that are used as training targets for each other.

While the concept of N2N enables the training of the DNN for PMRI without any fully sampled data, to the best of our knowledge, the prior work is based on using pre-estimated CSMs. Our SPICE method does not require pre-scan calibration, instead using the N2N framework for joint reconstruction and CSM estimation without any groundtruth.

3 Proposed Method

3.1 SPICE Model

Our SPICE method takes multicoil undersampled measurements as its input and produces the reconstructed images and CSMs at its output. As illustrated in Fig. 1, SPICE consists of two modules: (a) a **CSM estimation module** that uses information extracted from the raw measurements, and (b) a **DMBA-based MRI reconstruction module** that

forms reconstructed images from the input measurements and the estimated CSMs. Our training procedure uses a pair of multicoil undersampled measurement $\{(\mathbf{y}_i, \mathbf{y}'_i)\}_i$ which are acquired from the same object

$$\mathbf{y}_i = \mathbf{A}_i \mathbf{x}_i + \mathbf{e}_i \quad \text{and} \quad \mathbf{y}'_i = \mathbf{A}'_i \mathbf{x}_i + \mathbf{e}'_i, \quad (6)$$

where $(\mathbf{A}_i, \mathbf{A}'_i)$ and $(\mathbf{e}_i, \mathbf{e}'_i)$ denote distinct forward operators and noise vectors, respectively. The measurements \mathbf{y}_i and \mathbf{y}'_i can correspond to two subsets extracted from a single acquisition [17] or two separate MRI acquisitions. Note that our training procedure does not require any ground-truth images or known CSMs.

3.2 Coil Sensitivity Estimation Module

Let $\hat{\mathbf{y}}$ be an input measurement and \mathbf{P} the corresponding sampling matrix. The coil sensitivity estimation module forms CSMs from the *uncalibrated* multicoil measurements by performing three steps: (a) the ACS regions of the undersampled measurements are extracted, which are represented as \mathbf{y}_{ACS} ; (b) \mathbf{y}_{ACS} is mapped back to the image domain by applying the zero-filled inverse Fourier transform $\mathbf{p}^0 = \mathbf{F}^H(\mathbf{y}_{\text{ACS}})$; (c) \mathbf{p}^0 is fed into a CNN \mathbf{P}_φ with trainable parameters $\varphi \in \mathbb{R}^q$ to obtain estimated CSMs: $\hat{\mathbf{S}} = \mathbf{P}_\varphi(\mathbf{p}^0)$. (d) Finally, the estimated sensitivity maps $\hat{\mathbf{S}}$ are normalized by dividing their root-square-of-sum (RSS) to ensure that $\hat{\mathbf{S}}^H \hat{\mathbf{S}} = \mathbf{I}$.

3.3 Image Reconstruction Module

The image reconstruction module of SPICE is a DU model based on RED [41]. It forms the image iteratively by integrating information from CNN \mathbf{R}_θ with learnable parameters $\theta \in \mathbb{R}^p$ and imposing consistency between the predicted and the raw k-space measurements via ∇g . Let $\hat{\mathbf{c}}^0 = \mathbf{F}^H \hat{\mathbf{y}}$ represent the initial image, and $K \geq 1$ be the total number of DU layers, The steps of SPICE are given by

$$\mathbf{c}^{k+1} = \mathbf{c}^k - \underbrace{\gamma^k (\nabla g(\mathbf{c}^k, \mathbf{y}))}_{\text{Data Consistency}} + \underbrace{\tau^k \mathbf{S} \mathbf{R}_\theta^k(\mathbf{S}^H \mathbf{c}^k)}_{\text{Regularization}}, \quad (7)$$

where τ^k and γ^k are learnable parameters, \mathbf{c}^k represents the intermediate *multicoil* images in the k th step, and

$$\nabla g(\mathbf{c}^k, \mathbf{y}) = \mathbf{F}^H \mathbf{P}^H (\mathbf{P} \mathbf{F} \mathbf{c}^k - \mathbf{y}). \quad (8)$$

The CNN \mathbf{R}_θ^k in (7) takes a single image as an input, requiring \mathbf{S}^H and \mathbf{S} for fusing multiple images into a single image and expanding a single image into multiple images, respectively. The final reconstructed image \mathbf{x} can be obtained from the output of the last step as $\mathbf{x} = \mathbf{S}^H \mathbf{c}^K$. It is worth noting that unlike existing DU methods that rely on pre-calibrated \mathbf{S} [14–17], SPICE trains a \mathbf{S} calibration network simultaneously with the image reconstruction network.

3.4 Self-supervised Training Procedure

We use standard stochastic gradient method to jointly optimize $\{\theta_k\}_{k=1}^K$ and φ by minimizing the loss function

$$\text{Loss} = \text{Loss}_{\text{rec}} + \lambda \cdot \text{Loss}_{\text{smooth}}, \quad (9)$$

where λ is a regularization parameter.

Loss_{rec} seeks to map each \mathbf{y}_i and the corresponding \mathbf{y}'_i to each other. The key idea here is to map the reconstructed images back to the k-space domain by applying the forward operator of the training target. For example, one can map \mathbf{x}_i back to the k-space domain by applying the forward operator \mathbf{A}'_i then penalize the discrepancy between the resulting measurements $\mathbf{A}'_i \mathbf{x}_i$ and raw measurements \mathbf{y}'_i . Here, the CSMs \mathbf{S}_i in \mathbf{A}_i are estimated by the coil sensitivity estimation module after feeding \mathbf{y}_i as the input. The formulation of Loss_{rec} is

$$\text{Loss}_{\text{rec}} = \frac{1}{N} \sum_{i=1}^N \mathcal{L}_{\text{rec}}(\mathbf{A}'_i \mathbf{x}_i, \mathbf{y}'_i) + \mathcal{L}_{\text{rec}}(\mathbf{A}_i \mathbf{x}'_i, \mathbf{y}_i), \quad (10)$$

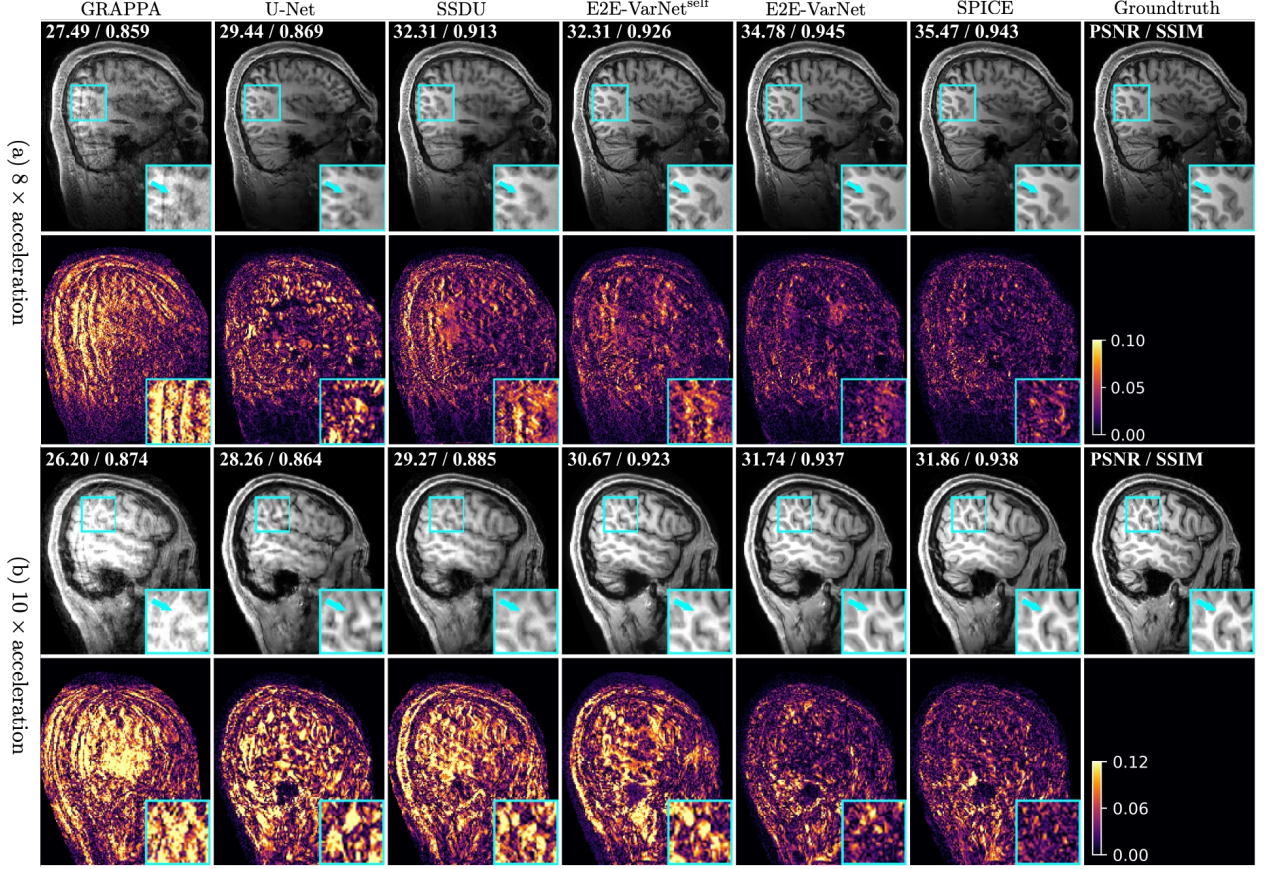


Figure 3: Visual and quantitative evaluation on real data corresponding to $8\times$ and $10\times$ acceleration rates. The top-right corner of each image provides the PSNR and SSIM values with respect to the ground-truth. We highlight the visually significant differences using zoom views and error maps. The visually important differences are highlighted using arrows. U-Net, E2E-VarNet^{self}, and SPICE in the figure are based on self-supervised learning. E2E-VarNet is supervised learning method trained using groundtruth. SPICE achieves the best performance compared to the baseline methods by jointly performing image reconstruction and CSM estimation with an end-to-end self-supervised training. Note how compared to other methods, SPICE recovers sharper images and reduces artifacts, even achieving comparable performance to the supervised learning method.

where \mathbf{x}'_i is the reconstructed image when \mathbf{y}'_i is the input measurement, and \mathcal{L}_{rec} denotes the ℓ_2 -norm. During minimization, Loss_{rec} enforces the accuracy between the predicted and the raw measurements, but it can also generate non-smooth CSMs that are not physically realistic and cause overfitting. Therefore, we include $\text{Loss}_{\text{smooth}}$, a smoothness regularization for CSMs, to impose smoothness within the field of view (FOV) region of estimated CSMs.

$$\text{Loss}_{\text{smooth}} = \frac{1}{N} \sum_{i=1}^N \left\| \mathbf{D}(\mathbf{S})_i^{\text{FOV}} \right\|_2^2. \quad (11)$$

The combination of Loss_{rec} and $\text{Loss}_{\text{smooth}}$ can enable the optimization on the measurement domain and the stability of CSMs, thus it is named as a smoothness-enhanced measurement domain loss function.

4 EXPERIMENTAL VALIDATION

We now present the numerical validation of SPICE on *in-vivo* MRI data. The results show that SPICE achieves state-of-the-art performance at highly accelerated acquisition settings.

4.1 Data Preparation

Dateset: The data acquisition was performed on a Siemens 3T Prisma scanner (Siemens Healthcare, Erlangen, Germany) with a 32-channel Head coil. Images were collected with Sagittal T1 magnetization-prepared rapid gradient-echo (MPRAGE) sequence. The acquisition parameters were as follows: repetition time (TR) = 2400 ms, echo time (TE) = 2.62 ms, inversion time (TI) = 1000 ms, flip angle (FA) = 8 degrees, FOV = 256 mm \times 256 mm, voxel size = 1 \times 1 \times 1 mm, slices per slab = 176, slice and phase resolution = 100% and slice and phase partial Fourier off. A 2 \times oversampling was used in the frequency encoding direction, and the asymmetric echo was turned on to allow short TE. All the data were fully-sampled measurements acquired with GRAPPA turned off, and the total acquisition time was 10 minutes and 16 seconds. The groundtruth images were obtained from fully-sampled multi-coil k-space measurements using the coil sensitivity maps from ESPIRiT. Upon the approval of our Institutional Review Board, we used brain MRI data from 14, 1, and 5 participants in this study for training, validation, and testing, respectively.

Sampling masks: The multi-coil k-space data were retrospectively undersampled using 1D Cartesian equispaced sampling masks with ACS lines. The sampling strategy is based on the clinical-used 2 \times acceleration sampling pattern, which is acquired with GRAPPA $R = 2$ in phase encoding (PE) direction with 24 ACS lines. As shown in Fig. 2, we conducted our experiments for acceleration factors $R = 4, 6, 8$ and 10 with 1D equispaced Cartesian masks, that contain 24, 24, 8 and 5 ACS lines respectively. They correspond to the retrospective sampling rates of 32%, 24%, 15% and 12%.

Acceleration Factor	4 \times acceleration			6 \times acceleration		
Method	PSNR \uparrow	SSIM \uparrow	NMSE \downarrow	PSNR \uparrow	SSIM \uparrow	NMSE \downarrow
Zero-Filled	18.27 \pm 1.672 \star	0.775 \pm 0.3842 \star	0.6212 \pm 0.3460 \star	18.07 \pm 1.694 \star	0.745 \pm 0.0419 \star	0.6532 \pm 0.3732 \star
Total variation [28]	38.54 \pm 1.467 \star	0.966 \pm 0.0071 \star	0.0039 \pm 0.0012 \star	32.04 \pm 1.221 \star	0.916 \pm 0.0171 \star	0.0039 \pm 0.0012 \star
GRAPPA [1]	39.74 \pm 1.386 \star	0.968 \pm 0.0073 \star	0.0037 \pm 0.0010 \star	33.03 \pm 1.405 \star	0.908 \pm 0.0051 \star	0.0463 \pm 0.0128 \star
U-Net [30]	36.18 \pm 1.405 \star	0.957 \pm 0.0051 \star	0.0092 \pm 0.0029 \star	33.99 \pm 1.381 \star	0.934 \pm 0.0123 \star	0.0151 \pm 0.0036 \star
SSDU [17]	37.49 \pm 1.662 \star	0.969 \pm 0.0076 \star	0.0071 \pm 0.0048 \star	34.33 \pm 2.099 \star	0.944 \pm 0.0114 \star	0.0167 \pm 0.0199 \star
E2E-VarNet ^{self} [20]	39.87 \pm 1.765 \star	0.981 \pm 0.0051 \star	0.0039 \pm 0.0022 \star	36.84 \pm 1.525 \star	0.965 \pm 0.0081 \star	0.0076 \pm 0.0033 \star
SPICE	41.60 \pm 1.457	0.981 \pm 0.0053	0.0026 \pm 0.0012	38.33 \pm 1.419	0.967 \pm 0.0081	0.0056 \pm 0.0021
E2E-VarNet [20]	40.64 \pm 1.564 \star	0.982 \pm 0.0050 \star	0.0032 \pm 0.0013 \star	37.51 \pm 1.595 \star	0.968 \pm 0.0058 \star	0.0068 \pm 0.0030 \star

Acceleration Factor	8 \times acceleration			10 \times acceleration		
Method	PSNR \uparrow	SSIM \uparrow	NMSE \downarrow	PSNR \uparrow	SSIM \uparrow	NMSE \downarrow
Zero-Filled	17.55 \pm 1.510 \star	0.721 \pm 0.0433 \star	0.7197 \pm 0.3737 \star	16.90 \pm 1.328 \star	0.701 \pm 0.0450 \star	0.8209 \pm 0.3865 \star
Total variation [28]	26.74 \pm 1.459 \star	0.859 \pm 0.0256 \star	0.0637 \pm 0.0236 \star	26.01 \pm 1.255 \star	0.849 \pm 0.0201 \star	0.0794 \pm 0.0270 \star
GRAPPA [1]	28.02 \pm 1.365 \star	0.877 \pm 0.0223 \star	0.0610 \pm 0.0234 \star	26.10 \pm 1.165 \star	0.859 \pm 0.0197 \star	0.0718 \pm 0.0262 \star
U-Net [30]	31.05 \pm 1.521 \star	0.887 \pm 0.0178 \star	0.0332 \pm 0.0113 \star	29.62 \pm 1.375 \star	0.892 \pm 0.0190 \star	0.0396 \pm 0.0128 \star
SSDU [17]	32.68 \pm 1.550 \star	0.919 \pm 0.0149 \star	0.0216 \pm 0.0135 \star	31.02 \pm 1.571 \star	0.894 \pm 0.0183 \star	0.0321 \pm 0.0231 \star
E2E-VarNet ^{self} [20]	33.04 \pm 1.543 \star	0.932 \pm 0.0130 \star	0.0174 \pm 0.0055 \star	31.14 \pm 1.762 \star	0.916 \pm 0.0160 \star	0.0257 \pm 0.0089 \star
SPICE	35.53 \pm 1.384	0.947 \pm 0.0114	0.0104 \pm 0.0031	33.37 \pm 1.433	0.927 \pm 0.0153	0.0179 \pm 0.0061
E2E-VarNet [20]	34.86 \pm 1.557 \star	0.950 \pm 0.0112 \star	0.0122 \pm 0.0057 \star	31.87 \pm 1.524 \star	0.931 \pm 0.0157 \star	0.0221 \pm 0.0083 \star

Statistically significant differences compared with SPICE are marked ($P\star < 0.05$).

Table 1: Quantitative evaluation (Mean \pm Standard Deviation) of SPICE. Note how SPICE achieves the best performance against other self-supervised baselines and comparable performance relative to the supervised method.

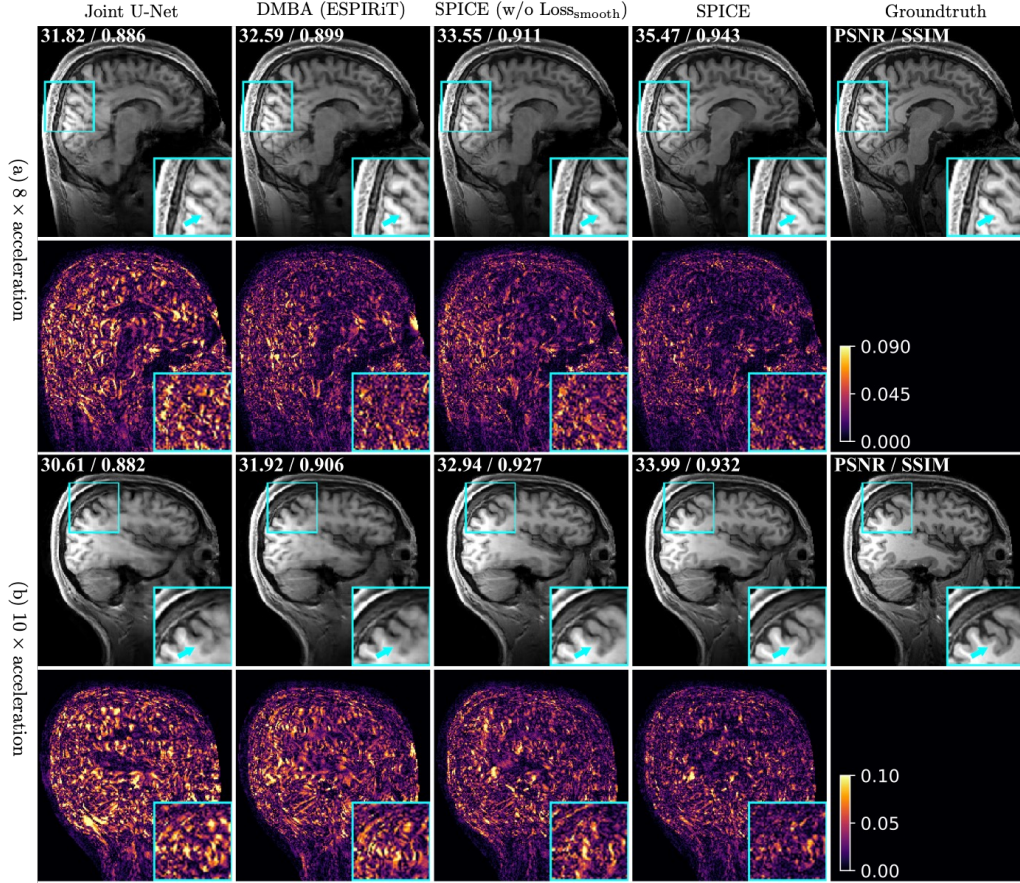


Figure 4: Quantitative evaluation of SPICE on experimentally-collected data at $8\times$ and $10\times$ acceleration rates. The top-right corner of each image provides the PSNR and SSIM values with respect to the ground-truth. We highlight visually significant differences using zoom views and error maps. This figure shows that the DMBA, CSM estimator, and CSM smoothness regularization of SPICE play important role in enhancing both quantitative and visual performance in terms of both artifact-removal and sharpness.

4.2 Evaluation Metrics

We used widely-used quantitative metrics, peak signal-to-noise ratio (PSNR), measured in dB, structural similarity index (SSIM), and the normalized mean squared error (NMSE), relative the groundtruth images obtained from the fully-sampled data. Images are compared within a FOV obtained by center cropping images to 255×255 . The quantitative results were statistically analyzed by comparing SPICE to other image reconstruction methods. We used the non-parametric Friedman’s test and the post-hoc test of the original FDR method of Benjamini and Hochberg [56]. The statistical analysis was performed using GraphPad Prism 9 (Version 9.3.1 for macOS, GraphPad Software, San Diego, CA, USA). Statistical significance was defined as $P < 0.05$.

4.3 Implementation

In our experiment, all CNNs in SPICE are based on U-Net [30] and implemented using PyTorch [57]. To process complex-valued data, we reshape all the complex-valued images by splitting their real and imaginary parts and concatenating them into the channel ($= 2$) dimensions. The total number of unrolling layers K in (7) is 8 and the regularization parameter λ in (9) is 0.01. The initial values we used in (7) is $\gamma^0 = 1$ and $\tau^0 = 0.1$. We used Adam as the optimizer with a learning rate 0.001 for the initial 30 epochs and 0.0001 for the rest. We performed all our experiments

on a machine equipped with an Intel Xeon Gold 6130 Processor and an NVIDIA GeForce RTX 3090 GPU.

4.4 Comparisons

4.4.1 Baseline Methods

We selected several well-known methods as references to compare the performance of SPICE:

- *TV (with ESPIRiT)*: The traditional TV regularized image reconstruction [28].
- *GRAPPA*: Traditional GRAPPA [1] that linearly interpolates missing k-space points using nearby acquired k-space points along the coil dimension.
- *U-Net*: The U-Net architecture [30] trained to maximize SSIM between the reconstructed image and the image obtained using GRAPPA on the same amount of measurements as SPICE.
- *SSDU*: A well-known self-supervised learning method [17] that trains a DU network by dividing each k-space MRI acquisition into two subsets and using them as training targets for each other.
- *E2E-VarNet^{self}*: A well-known DMBA architecture from [20] for end-to-end PMRI reconstruction and automatic coil estimation. The *E2E-VarNet^{self}* variant was trained without groundtruth similarly to U-Net.
- *E2E-VarNet*: An idealized variant of method from [20] trained using SSIM on fully-sampled groundtruth data. E2E-VarNet shows the upper bound on performance achievable by the self-supervised variants of the method.

All the CSMs used in TV (with ESPIRiT), U-Net, and SSDU are pre-estimated using ESPIRiT [4]. We observed that when the number of ACS lines is less than 24, reconstruction using the CSMs estimated by ESPIRiT are of poor quality. Therefore, we use 24 ACS lines for estimating CSMs with ESPIRiT to be used in TV, U-Net, and SSDU.

4.4.2 Ablation Study

We also performed an ablation study to highlight the influence of the DMBA module, the CSMs estimation module, and the CSMs smoothness regularization within SPICE. We compared the original SPICE model with three different models as follows:

- *Joint U-Net*: We replace the DMBA module of SPICE with U-Net to show the benefit of using a DMBA.
- *DMBA (ESPIRiT)*: We use the same DMBA as SPICE but use ESPIRiT on undersampled measurements to replace the CSM estimation module of SPICE.
- *SPICE (w/o $\text{Loss}_{\text{smooth}}$)*: SPICE trained without the CSMs smoothness regularization loss $\text{Loss}_{\text{smooth}}$ in (11).

4.4.3 Evaluation of Coil Sensitivity Maps Estimation

In order to evaluate the quality of the estimated CSMs, we use CSMs estimated by the proposed and baseline methods within the iterative TV reconstruction. We use `fminbound` in the `scipy.optimize` toolbox to identify the optimal regularization parameters for TV.

4.5 Results and Discussion

Fig. 3 illustrates the results of image reconstruction for acceleration rates $R = 8$ (top) and $R = 10$ (bottom). TV (with ESPIRiT) and GRAPPA contain blurring and ghosting artifacts, especially at higher acceleration rates. While U-Net has better performance than TV (with ESPIRiT) and GRAPPA by learning the prior from data, SSDU and E2E-VarNet^{self} outperform it due to their model-based DL architectures. E2E-VarNet^{self} performs joint CSMs estimation, which enables it to do better than SSDU. Yet, it still suffers from some blurring, due to the use of sub-optimal training target obtained by using GRAPPA. The supervised learning baseline E2E-VarNet and our proposed method

Acceleration Factor Method	4× acceleration			6× acceleration		
	PSNR ↑	SSIM ↑	NMSE ↓	PSNR ↑	SSIM ↑	NMSE ↓
Joint U-Net	36.80 ± 1.502★	0.959 ± 0.0098★	0.0079 ± 0.0024★	33.95 ± 1.493★	0.934 ± 0.0144★	0.0153 ± 0.0051★
DMBA (ESPIRiT)	37.97 ± 1.424★	0.968 ± 0.0090★	0.0612 ± 0.0026★	35.24 ± 1.270★	0.945 ± 0.0131★	0.0112 ± 0.0031★
SPICE (w/o Loss _{smooth})	41.28 ± 1.446★	0.979 ± 0.0059★	0.0028 ± 0.0014★	37.93 ± 1.435★	0.963 ± 0.0085★	0.0062 ± 0.0028★
SPICE	41.60 ± 1.457	0.981 ± 0.0053	0.0026 ± 0.0012	38.33 ± 1.419	0.967 ± 0.0081	0.0056 ± 0.0021

Acceleration Factor Method	8× acceleration			10× acceleration		
	PSNR ↑	SSIM ↑	NMSE ↓	PSNR ↑	SSIM ↑	NMSE ↓
Joint U-Net	31.01 ± 1.538★	0.896 ± 0.0199★	0.0317 ± 0.0115★	29.32 ± 1.438★	0.863 ± 0.0232★	0.0472 ± 0.0197★
DMBA (ESPIRiT)	31.68 ± 1.521★	0.905 ± 0.0167★	0.0255 ± 0.0075★	26.83 ± 1.521★	0.854 ± 0.0185★	0.1380 ± 0.0495★
SPICE (w/o Loss _{smooth})	34.83 ± 1.473★	0.945 ± 0.0144★	0.0127 ± 0.0053★	32.62 ± 1.463★	0.921 ± 0.0168★	0.0211 ± 0.0087★
SPICE	35.53 ± 1.384	0.947 ± 0.0114	0.0104 ± 0.0031	33.37 ± 1.433	0.927 ± 0.0153	0.0179 ± 0.0061

Statistically significant differences compared with SPICE are marked ($P^* < 0.05$).

Table 2: Quantitative evaluation (Mean ± standard deviation) using four distinct implementations of SPICE. This table shows the influence of the DMBA reconstruction module, the CSM estimation module, and the smooth term in the loss function.

SPICE achieve significant improvements compared to other methods. Overall, our proposed method SPICE can provide the best performance in artifact removal and sharpness compared to all of the self-supervised baseline methods.

Table 1 summarizes quantitative results of all the evaluated methods. Table 1 shows that SPICE achieves the highest PSNR, highest SSIM, and lowest NMSE values compared to other methods over all considered acceleration rate. Moreover, our method achieves very competitive performance with a state-of-the-art supervised learning method E2E-VarNet. Note that E2E-VarNet also utilizes the joint learning of unrolling network and CSM estimation network. Statistical analysis of PSNR, SSIM, and NMSE values in Table 1 also highlights that SPICE can achieve statistically significant results compared to the self-supervised image reconstruction baseline methods.

Figure 4 illustrates reconstruction results of the ablation study on 8× and 10× acceleration. Figure 4 shows that the DMBA model, CSM estimator, and CSM smoothness regularization of SPICE improve the imaging quality. Table 2 presents the results of an ablation study showing the influence of each module of our SPICE model and the effectiveness of Loss_{smooth} in the proposed self-supervised loss function (9). As can be seen, Joint U-Net obtains the worst performance, due to the U-Net model not using the PMRI measurement model. The results suggest that pre-estimated CSMs generated with ESPIRiT used in DMBA lead to sub-optimal performance in all acceleration rates, especially with limited ACS lines. Note that at high acceleration rates (8× and 10×), even the CSMs pre-estimated with ESPIRiT on 4× accelerated data, the performance is still much worse than that of the joint CSM learning methods. The results of SPICE (w/o Loss_{smooth}) and SPICE show that CSM smoothness regularization plays an important role in the reconstruction. Statistical analysis of quantitative values in Table 2 highlights that SPICE achieves statistically significant results compared to other methods.

Fig. 5 illustrates the performance of the estimated CSMs. We use ESPIRiT and SPICE to estimate CSMs from data at various accelerated acquisition rates (from 4× to 10×). Estimated CSMs are then used within TV reconstruction from data corresponding to 4× accelerated acquisition rate. The reconstructed images are quantitatively evaluated using PSNR and SSIM values relative to the ground-truth images. The top row of Fig. 5 illustrates the TV reconstruction results equipped with CSMs estimated from different ACS data and different methods. The bottom row of Fig. 5 illustrates the visualization of CSMs of one specific coil. Note that, even with CSMs estimated by SPICE from 5 ACS lines, the following TV reconstruction can achieve better performance than ESPIRiT CSMs (generated from 24 ACS lines).

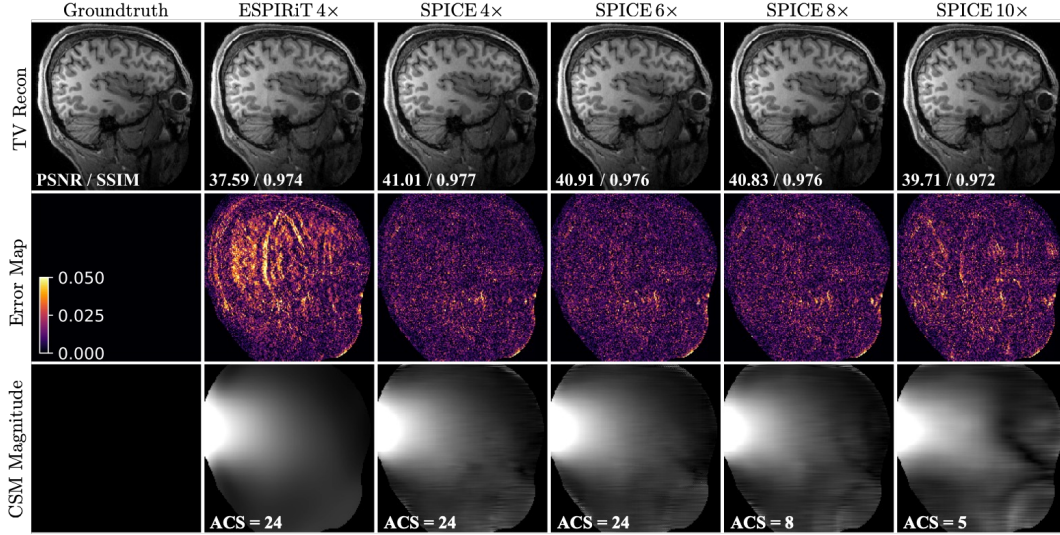


Figure 5: Evaluation of CSMs estimated by SPICE at various acceleration rates. The third rows shows the sensitivity map of the 10th coil estimated by SPICE and ESPIRiT. The first row shows the results from using these CSMs within TV reconstruction at acceleration rate $R = 4$. The bottom-left corner of each image provides PSNR/SSIM with respect to the ground-truth. Visually significant differences are highlighted using error maps.

5 Conclusion

We introduce SPICE as a self-supervised learning method that uses pairs of noisy and undersampled k-space measurements of the same object to train a model for joint MRI reconstruction and automatic coil sensitivity calibration. The key benefit of SPICE is that it is trained directly in k-space without any fully-sampled groundtruth data, which makes it broadly applicable to when groundtruth is impossible or difficult to obtain. We presented a set of numerical results on real PMRI data showing that despite being trained on noisy undersampled data, SPICE can reconstruct high-quality images and CSMs in highly undersampled settings. Our results also highlight the importance of different modules of SPICE—including the DMBA, the CSM estimation, and the SPICE training loss—on the final performance of the method. Our results indicate that the synergistic combination of all these factors enables SPICE to outperform other self-supervised learning methods and match the performance of the well-known E2E-VarNet trained on fully-sampled groundtruth data.

Acknowledgements

Research reported in this publication was supported by the NSF CAREER award under CCF-2043134.

References

- [1] M. A. Griswold, P. M. Jakob, R. M. Heidemann, M. Nittka, V. Jellus, J. Wang, B. Kiefer, and A. Haase, “Generalized autocalibrating partially parallel acquisitions (GRAPPA),” *Magn. Reson. Med.*, vol. 47, no. 6, pp. 1202–1210, Jun. 2002.
- [2] D. K. Sodickson and W. J. Manning, “Simultaneous acquisition of spatial harmonics (SMASH): Fast imaging with radiofrequency coil arrays,” *Magn. Reson. Med.*, vol. 38, no. 4, pp. 591–603, Oct. 1997.
- [3] K. P. Pruessmann, M. Weiger, M. B. Scheidegger, and P. Boesiger, “SENSE: Sensitivity encoding for fast MRI,” *Magn. Reson. Med.*, vol. 42, no. 5, pp. 952–962, Nov. 1999.

- [4] M. Uecker, P. Lai, M. J. Murphy, P. Virtue, M. Elad, J. M. Pauly, S. S. Vasanawala, and M. Lustig, “ESPIRiT—an eigenvalue approach to autocalibrating parallel MRI: Where SENSE meets GRAPPA,” *Magn. Reson. Med.*, vol. 71, no. 3, pp. 990–1001, Mar. 2014.
- [5] M. Lustig, D. Donoho, and J. M. Pauly, “Sparse MRI: The application of compressed sensing for rapid MR imaging,” *Magn. Reson. Med.*, vol. 58, no. 6, pp. 1182–1195, 2007.
- [6] J. C. Ye, “Compressed sensing MRI: A review from signal processing perspective,” *BMC Biomed. Eng.*, vol. 1, no. 1, p. 8, Dec. 2019.
- [7] G. Ongie, A. Jalal, C. A. Metzler, R. G. Baraniuk, A. G. Dimakis, and R. Willett, “Deep learning techniques for inverse problems in imaging,” *IEEE J. Sel. Areas Inf. Theory*, vol. 1, no. 1, pp. 39–56, 2020.
- [8] F. Knoll, K. Hammernik, C. Zhang, S. Moeller, T. Pock, D. K. Sodickson, and M. Akcakaya, “Deep-learning methods for parallel magnetic resonance imaging reconstruction: A survey of the current approaches, trends, and issues,” *IEEE Signal Process. Mag.*, vol. 37, no. 1, pp. 128–140, 2020.
- [9] J. Montalt-Tordera, V. Muthurangu, A. Hauptmann, and J. Steeden, “Machine learning in magnetic resonance imaging: image reconstruction,” *Physica Medica*, vol. 83, pp. 79–87, 2021.
- [10] K. H. Jin, M. T. McCann, E. Froustey, and M. Unser, “Deep Convolutional Neural Network for Inverse Problems in Imaging,” *IEEE Trans. on Image Process.*, vol. 26, no. 9, pp. 4509–4522, Sep. 2017.
- [11] B. Zhu, J. Z. Liu, S. F. Cauley, B. R. Rosen, and M. S. Rosen, “Image reconstruction by domain-transform manifold learning,” *Nature*, vol. 555, no. 7697, pp. 487–492, Mar. 2018.
- [12] K. Hammernik, J. Schlemper, C. Qin, J. Duan, R. M. Summers, and D. Rueckert, “Systematic evaluation of iterative deep neural networks for fast parallel MRI reconstruction with sensitivity-weighted coil combination,” *Magn. Reson. Med.*, p. mrm.28827, Jun. 2021.
- [13] D. Liang, J. Cheng, Z. Ke, and L. Ying, “Deep magnetic resonance image reconstruction: Inverse problems meet neural networks,” *IEEE Signal Process. Mag.*, vol. 37, no. 1, pp. 141–151, Jan. 2020.
- [14] J. Duan, J. Schlemper, C. Qin, C. Ouyang, W. Bai, C. Biffi, G. Bello, B. Statton, D. P. O’Regan, and D. Rueckert, “VS-Net: Variable Splitting Network for Accelerated Parallel MRI Reconstruction,” in *Proc. Medical Image Computing and Computer-Assisted Intervention*, vol. 11767. Cham: Springer International Publishing, 2019, pp. 713–722.
- [15] H. K. Aggarwal, M. P. Mani, and M. Jacob, “MoDL: Model-Based Deep Learning Architecture for Inverse Problems,” *IEEE Trans. Med. Imaging*, vol. 38, no. 2, pp. 394–405, Feb. 2019.
- [16] K. Hammernik, T. Klatzer, E. Kobler, M. P. Recht, D. K. Sodickson, T. Pock, and F. Knoll, “Learning a variational network for reconstruction of accelerated MRI data,” *Magn. Reson. Med.*, vol. 79, no. 6, pp. 3055–3071, 2018.
- [17] B. Yaman, S. A. H. Hosseini, S. Moeller, J. Ellermann, K. Uğurbil, and M. Akçakaya, “Self-supervised learning of physics-guided reconstruction neural networks without fully sampled reference data,” *Magn. Reson. Med.*, vol. 84, no. 6, pp. 3172–3191, 2020.
- [18] M. Arvinte, S. Vishwanath, A. H. Tewfik, and J. I. Tamir, “Deep J-Sense: Accelerated MRI reconstruction via unrolled alternating optimization,” *arXiv:2103.02087 [cs, eess]*, Apr. 2021.
- [19] Y. Jun, H. Shin, T. Eo, and D. Hwang, “Joint deep model-based MR image and coil sensitivity reconstruction network (joint-icnet) for fast MRI,” in *Proc. IEEE Conf. Comput. Vis. Pattern Recognit.*, 2021, pp. 5270–5279.
- [20] A. Sriram, J. Zbontar, T. Murrell, A. Defazio, C. L. Zitnick, N. Yakubova, F. Knoll, and P. Johnson, “End-to-end variational networks for accelerated MRI reconstruction,” in *Proc. Medical Image Computing and Computer-Assisted Intervention*, 2020, pp. 64–73.

- [21] B. Yaman, S. A. H. Hosseini, S. Moeller, J. Ellermann, K. Uğurbil, and M. Akçakaya, “Self-supervised physics-based deep learning mri reconstruction without fully-sampled data,” in *Proc. Int. Symp. Biomedical Imaging*. IEEE, 2020, pp. 921–925.
- [22] M. Akçakaya, B. Yaman, H. Chung, and J. C. Ye, “Unsupervised Deep Learning Methods for Biological Image Reconstruction,” *arXiv:2105.08040 [physics]*, May 2021.
- [23] J. Lehtinen, J. Munkberg, J. Hasselgren, S. Laine, T. Karras, M. Aittala, and T. Aila, “Noise2Noise: Learning image restoration without clean data,” in *Proc. Int. Conf. Mach. Learn.*, 2018.
- [24] C. Eldeniz, W. Gan, S. Chen, T. J. Fraum, D. R. Ludwig, Y. Yan, J. Liu, T. Vahle, U. Krishnamurthy, U. S. Kamilov, and H. An, “Phase2Phase: Respiratory Motion-Resolved Reconstruction of Free-Breathing Magnetic Resonance Imaging Using Deep Learning Without a Ground Truth for Improved Liver Imaging,” *Invest. Radiol.*, vol. Publish Ahead of Print, May 2021.
- [25] W. Gan, Y. Sun, C. Eldeniz, J. Liu, H. An, and U. S. Kamilov, “Deep Image Reconstruction Using Unregistered Measurements Without Groundtruth,” in *Proc. Int. Symp. Biomedical Imaging*. Nice, France: IEEE, Apr. 2021, pp. 1531–1534.
- [26] J. Liu, Y. Sun, C. Eldeniz, W. Gan, H. An, and U. S. Kamilov, “RARE: Image Reconstruction Using Deep Priors Learned Without Groundtruth,” *IEEE J. Sel. Top. Signal Process.*, vol. 14, no. 6, pp. 1088–1099, Oct. 2020.
- [27] W. Gan, Y. Hu, C. Eldeniz, J. Liu, Y. Chen, H. An, and U. S. Kamilov, “SS-JIRCS: Self-supervised joint image reconstruction and coil sensitivity calibration in parallel mri without ground truth,” in *Proc. IEEE Int. Conf. Comp. Vis. Workshops*, 2021, pp. 4048–4056.
- [28] K. T. Block, M. Uecker, and J. Frahm, “Undersampled radial mri with multiple coils. iterative image reconstruction using a total variation constraint,” *Magn. Reson. Med.*, vol. 57, no. 6, pp. 1086–1098, 2007.
- [29] G. Wang, J. C. Ye, and B. De Man, “Deep learning for tomographic image reconstruction,” *Nat. Mach. Intell.*, vol. 2, no. 12, pp. 737–748, Dec. 2020.
- [30] O. Ronneberger, P. Fischer, and T. Brox, “U-net: Convolutional networks for biomedical image segmentation,” in *Proc. Medical Image Computing and Computer-Assisted Intervention*, 2015, pp. 234–241.
- [31] D. Lee, J. Yoo, and J. C. Ye, “Deep residual learning for compressed sensing MRI,” in *Proc. Int. Symp. Biomedical Imaging*. Melbourne, Australia: IEEE, Apr. 2017, pp. 15–18.
- [32] S. Wang, Z. Su, L. Ying, X. Peng, S. Zhu, F. Liang, D. Feng, and D. Liang, “Accelerating magnetic resonance imaging via deep learning,” in *Proc. Int. Symp. Biomedical Imaging*. Prague, Czech Republic: IEEE, Apr. 2016, pp. 514–517.
- [33] B. Zhu, J. Z. Liu, S. F. Cauley, B. R. Rosen, and M. S. Rosen, “Image reconstruction by domain-transform manifold learning,” *Nature*, vol. 555, no. 7697, pp. 487–492, Mar. 2018.
- [34] Y. Han, L. Sunwoo, and J. C. Ye, “K-Space Deep Learning for Accelerated MRI,” *IEEE Trans. Med. Imaging*, vol. 39, no. 2, pp. 377–386, Feb. 2020.
- [35] S. V. Venkatakrishnan, C. A. Bouman, and B. Wohlberg, “Plug-and-Play priors for model based reconstruction,” in *Proc. IEEE Glob. Conf. Signal Process. Inf. Process.*, Dec. 2013, pp. 945–948.
- [36] U. S. Kamilov, C. A. Bouman, G. T. Buzzard, and B. Wohlberg, “Plug-and-play methods for integrating physical and learned models in computational imaging,” *IEEE Signal Process. Mag.*, 2022, arXiv:2203.17061.
- [37] Y. Romano, M. Elad, and P. Milanfar, “The Little Engine That Could: Regularization by Denoising (RED),” *SIAM J. Imaging Sci.*, vol. 10, no. 4, pp. 1804–1844, Jan. 2017.

- [38] J. Schlemper, J. Caballero, J. V. Hajnal, A. N. Price, and D. Rueckert, “A Deep Cascade of Convolutional Neural Networks for Dynamic MR Image Reconstruction,” *IEEE Trans. Med. Imaging*, vol. 37, no. 2, pp. 491–503, Feb. 2018.
- [39] K. Hammernik, T. Klatzer, E. Kobler, M. P. Recht, D. K. Sodickson, T. Pock, and F. Knoll, “Learning a variational network for reconstruction of accelerated MRI data,” *Magn. Reson. Med.*, vol. 79, no. 6, pp. 3055–3071, 2018.
- [40] H. K. Aggarwal, M. P. Mani, and M. Jacob, “MoDL: Model-Based Deep Learning Architecture for Inverse Problems,” *IEEE Trans. Med. Imaging*, vol. 38, no. 2, pp. 394–405, Feb. 2019.
- [41] J. Liu, Y. Sun, W. Gan, X. Xu, B. Wohlberg, and U. S. Kamilov, “SGD-Net: Efficient Model-Based Deep Learning With Theoretical Guarantees,” *IEEE Trans. Comput. Imaging*, vol. 7, pp. 598–610, 2021.
- [42] M. Akçakaya, M. Steen, W. Sebastian, and U. Kâmil, “Scan-specific robust artificial-neural-networks for k-space interpolation (raki) reconstruction: Database-free deep learning for fast imaging,” *Magn. Reson. Med.*, vol. 81, no. 1, pp. 439–453, 2019.
- [43] L. Ying and J. Sheng, “Joint image reconstruction and sensitivity estimation in SENSE (JSSENSE),” *Magn. Reson. Med.*, vol. 57, no. 6, pp. 1196–1202, Jun. 2007.
- [44] M. Uecker, T. Hohage, K. T. Block, and J. Frahm, “Image reconstruction by regularized nonlinear inversion-Joint estimation of coil sensitivities and image content,” *Magn. Reson. Med.*, vol. 60, no. 3, pp. 674–682, Sep. 2008.
- [45] X. Peng, B. P. Sutton, F. Lam, and Z. Liang, “Deepsense: Learning coil sensitivity functions for sense reconstruction using deep learning,” *Magn. Reson. Med.*, vol. 87, no. 4, pp. 1894–1902, 2022.
- [46] G. Yiasemis, J. Sonke, C. Sánchez, and J. Teuwen, “Recurrent variational network: A deep learning inverse problem solver applied to the task of accelerated mri reconstruction,” in *Proc. IEEE Conf. Comput. Vis. Pattern Recognit.*, 2022, pp. 732–741.
- [47] G. Zeng, Y. Guo, J. Zhan, Z. Wang, Z. Lai, X. Du, X. Qu, and D. Guo, “A review on deep learning mri reconstruction without fully sampled k-space,” *BMC Med. Imaging*, vol. 21, no. 1, pp. 1–11, 2021.
- [48] M. Akçakaya, B. Yaman, H. Chung, and J. C. Ye, “Unsupervised deep learning methods for biological image reconstruction and enhancement: An overview from a signal processing perspective,” *IEEE Signal Process. Mag.*, vol. 39, no. 2, pp. 28–44, 2022.
- [49] J. Tachella, D. Chen, and M. Davies, “Sampling Theorems for Unsupervised Learning in Linear Inverse Problems,” *arXiv:2203.12513*, Mar. 2022.
- [50] J. Lehtinen, J. Munkberg, J. Hasselgren, S. Laine, T. Karras, M. Aittala, and T. Aila, “Noise2Noise: Learning image restoration without clean data,” in *Proc. Int. Conf. Mach. Learn.*, 2018.
- [51] A. Krull, T.-O. Buchholz, and F. Jug, “Noise2Void - Learning Denoising From Single Noisy Images,” in *Proc. IEEE Conf. Comput. Vis. Pattern Recognit.*, Jun. 2019, pp. 2124–2132.
- [52] D. Ulyanov, A. Vedaldi, and V. Lempitsky, “Deep image prior,” in *Proc. IEEE Conf. Comput. Vis. Pattern Recognit.*, 2018, pp. 9446–9454.
- [53] A. Bora, E. Price, and A. G. Dimakis, “Ambientgan: Generative models from lossy measurements,” in *Int. Conf. Learn. Represent.*, 2018.
- [54] D. Chen, J. Tachella, and M. E. Davies, “Equivariant imaging: Learning beyond the range space,” in *Proc. IEEE Conf. Comput. Vis. Pattern Recognit.*, 2021, pp. 4379–4388.
- [55] P. Huang, C. Zhang, X. Zhang, X. Li, L. Dong, and L. Ying, “Unsupervised deep unrolled reconstruction using regularization by denoising,” *arXiv preprint arXiv:2205.03519*, 2022.

- [56] Y. Benjamini and Y. Hochberg, “Controlling the false discovery rate: a practical and powerful approach to multiple testing,” *Journal of the Royal statistical society: series B (Methodological)*, vol. 57, no. 1, pp. 289–300, 1995.
- [57] A. Paszke, S. Gross, F. Massa, A. Lerer, J. Bradbury, G. Chanan, T. Killeen, Z. Lin, N. Gimeshein, L. Antiga *et al.*, “Pytorch: An imperative style, high-performance deep learning library,” *Advances in neural information processing systems*, vol. 32, 2019.